Optical Engineering

OpticalEngineering.SPIEDigitalLibrary.org

Fiber-optic temperature profiling for thermal protection system heat shields

Richard J. Black
Joannes M. Costa
Livia Zarnescu
Drew A. Hackney
Behzad Moslehi
Kara J. Peters

SPIE.

Richard J. Black, Joannes M. Costa, Livia Zarnescu, Drew A. Hackney, Behzad Moslehi, Kara J. Peters, "Fiber-optic temperature profiling for thermal protection system heat shields," *Opt. Eng.* **55**(11), 114101 (2016), doi: 10.1117/1.OE.55.11.114101.

Fiber-optic temperature profiling for thermal protection system heat shields

Richard J. Black,[a,*] Joannes M. Costa,[a] Livia Zarnescu,[a] Drew A. Hackney,[b] Behzad Moslehi,[a] and Kara J. Peters[b]
[a]Intelligent Fiber Optic Systems Corporation (IFOS), 2363 Calle Del Mundo, Santa Clara, California 95054, United States
[b]North Carolina State University, Department of Mechanical and Aerospace Engineering, Engineering Building 3, Raleigh, North Carolina 27695, United States

Abstract. To achieve better designs for spacecraft heat shields for missions requiring atmospheric aero-capture or entry/reentry, reliable thermal protection system (TPS) sensors are needed. Such sensors will provide both risk reduction and heat-shield mass minimization, which will facilitate more missions and enable increased payloads and returns. This paper discusses TPS thermal measurements provided by a temperature monitoring system involving lightweight, electromagnetic interference-immune, high-temperature resistant fiber Bragg grating (FBG) sensors with a thermal mass near that of TPS materials together with fast FBG sensor interrogation. Such fiber-optic sensing technology is highly sensitive and accurate, as well as suitable for high-volume production. Multiple sensing FBGs can be fabricated as arrays on a single fiber for simplified design and reduced cost. Experimental results are provided to demonstrate the temperature monitoring system using multisensor FBG arrays embedded in a small-size super-light ablator (SLA) coupon which was thermally loaded to temperatures in the vicinity of the SLA charring temperature. In addition, a high-temperature FBG array was fabricated and tested for 1000°C operation, and the temperature dependence considered over the full range (cryogenic to high temperature) for which silica fiber FBGs have been subjected. [DOI: 10.1117/1.OE.55.11.114101]

Keywords: thermal protection systems; thermal protection system; temperature sensing; fiber-optic sensing; fiber Bragg gratings.

Paper 160511P received Apr. 13, 2016; accepted for publication Sep. 2, 2016; published online Oct. 27, 2016; corrected Nov. 13, 2016.

1 Introduction

A thermal protection system (TPS) is an essential spacecraft subsystem that shields the vehicle structure and payload from the high heating loads encountered during launch and reentry. Moreover, the TPS is a single-point failure subsystem for any vehicle traveling at hypersonic speeds in an atmospheric environment. On the other hand, an effective TPS enables safe deployment of *in situ* science instruments using small probes[1] and landers as well as other instrumented systems. Currently, there are two types of TPS technology:

- Reusable
- Ablative

Reusable TPS applications typically are limited to relatively mild entry environments such as that of the space shuttle. No change in the mass or properties of the TPS material results from entry with a significant amount of energy being reradiated from the heated surface (usually using a surface coating with high emissivity) and the remainder conducted into the TPS material.

Ablative TPS applications include all NASA planetary entry probes to date. In contrast to reusable TPS, ablative TPS accommodate high heating rates and heat loads through phase change and mass loss. More specifically, an ablative TPS protects a vehicle via thermochemical phenomena, which include:

- an ablation process that lifts the hot shock layer gas away from the vehicle;
- heat absorption by the ablative material leaves the vehicle undamaged as the material ablates away;
- the creation of a char layer, which is an effective insulator and also effective at blocking radiated heat from the shock layer.[2]

There are several different types of ablative materials used for TPS but, in recent years, NASA has tended to use lightweight ablators such as:

- Phenolic impregnated carbon ablator (PICA): developed by NASA Ames Research Center (ARC) in the 1990s and used in the Stardust Sample Return Mission forebody heatshield[3,4] and the Mars Science Laboratory (MSL);[5,6]
- PICA-X: developed by SpaceX for the Dragon space capsule;
- Silicone impregnated reusable ceramic ablator (SIRCA): developed by NASA/ARC and used on the backshell of the Mars Pathfinder;[7]
- Superlight ablator (SLA): SLAs such as SLA-561 and SLA-741[8] composed of silicone resin with cork, phenolic microballoon, silica microballoon, and refractory fiber fillers were developed in the 1960s. Today, the best known SLA is SLA-561V,[9,10] which is a proprietary ablative (ablator packed in a honeycomb core) made by Lockheed Martin that has been used as the primary TPS material on the 70-deg sphere-cone entry vehicles sent to Mars by NASA (e.g., Viking

*Address all correspondence to: Richard J. Black, E-mail: rjb@ifos.com

and Pathfinder)[11] and on the backshell of the Stardust Sample Return Mission;

- Avcoat: manufactured by HR Textron and applied to the Apollo and reformulated for the Orion.[12]

Such TPS materials, while reasonably effective in certain applications, are often incompletely characterized and difficult to apply universally. There remains a need for new, well-characterized, more robust ablative TPS materials. Uncertainties in computational fluid dynamics (CFD) and material thermal response models, however, are significant and limit the ability to design and validate new and improved ablators for future space missions involving atmospheric reentry. Accordingly, validation by relevant ground (e.g., arc-jet test[13]) and flight data are critical. Appropriate TPS instrumentation can provide accurate, repeatable data during ground- and flight-testing. This, in turn, can provide needed traceability of TPS sizing and material performance[14,15] leading to higher fidelity models and design tools, which in turn will enable reduced risk and decreased TPS mass in future entry/reentry systems. Such improvements will enable certain space missions that are not otherwise feasible, and directly increase science payload and returns,[16] enabling, e.g., small probes to carry more, remain light, and become safer/less likely to burn up during reentry.

Until 2012, the majority of TPS flight data was acquired in the 1960s,[17] in support of Apollo, with later planetary/science mission vehicles, including Stardust, being largely unsuccessful.[13] The successful performance through "seven minutes of terror" of the MSL Entry, Descent, and Landing Instrumentation (MEDLI)[6] provided a very valuable stepping-stone toward alleviating the limited TPS flight data available.

There remains, however, a need to build upon and further improve the MEDLI instrumentation. Currently, thermocouples form a key part of instrumented plugs for heat shields such as the MEDLI[6] (see Fig. 1) and MEDLI2.[18] These thermocouples have limitations in terms of response speed and wiring required for each thermocouple. Multiplexed fiber-optic sensors, which are surprisingly resistant to a range of harsh environments,[19–22] have the potential to alleviate these problems—multiple sensors can be placed on a single-electromagnetic interference-immune optical fiber with TPS compatible thermal mass and have the potential for compact and minimally invasive integration into thermal protection structures[23] including small-size TPS plugs similar to those that were installed in the MSL heat shield (Fig. 1).

Fiber-optic sensors that can be used for high-temperature sensing include fiber Bragg gratings (FBGs)[19–22] and long period gratings (LPGs)[24–27] both reviewed in the Appendix as well as fiber Fabry–Pérot (FP)[28] sensors. FBG sensors allow for the greatest multiplexibility with arrays of many sensors supported on a single optical fiber of which only one end is required to be attached to instrumentation. While other sensor systems, such as LPGs, can be multiplexed, FBGs are significantly shorter in length, which allows for better spatial resolution in multiplexed sensor systems. The FBGs used in this study are 4 mm in length, compared to LPGs which can be in the 50-mm range.[27] Furthermore, in addition to thermal (multi-point temperature and heat-flux) sensing, grating-based sensor systems have a significant advantage in terms of multifunctionality in that they lend themselves to support of multiple sensors types that could find usage in both (a) a spacecraft's TPS such as dynamic strain/vibration/acceleration,[29] pressure,[30,31] and recession sensors, and (b) internal to a spacecraft, e.g., humidity.[27]

In this paper, we provide experimental results to demonstrate an IFOS-developed temperature monitoring system based on parallel processing FBG interrogation[20,29] and implemented for (a) a high-temperature FBG array operating to 1000°C and (b) two multisensor FBG arrays (total eight sensors) embedded in the 50 mm × 25 mm cross section of a small-size SLA coupon which was thermally loaded in multiple tests to temperatures ranging from 200 to 280°C. In particular, in Sec. 2, we describe sensor characterization with two example FBG arrays, one of them to 1000°C. In Sec. 3, we describe the design and integration of two sensor arrays into a small-size SLA TPS coupon. In Sec. 4, we describe the thermal loading of this coupon and provide measurement results. Conclusions are presented in Sec. 5. FBG sensor temperature dependence over the extreme temperature ranging from close to absolute zero to 1200°C is discussed in the Appendix.

2 Sensor Calibration

2.1 *Fiber Bragg Grating Temperature Dependence*

FBG-based temperature sensing is performed by tracking the (Bragg) wavelength reflected by the FBG. While it is commonly assumed in the literature that the Bragg wavelength dependence on temperature is linear, taking into account a quadratic correction[32] due to material dispersion,[33] $\mathrm{d}n(\lambda)/\mathrm{d}T$, leads to more accurate results over expanded temperature ranges. In particular, the change in Bragg wavelength $\delta\lambda_B$ with respect to Bragg wavelength λ_{Bo} at temperature T_o as a function of temperature $T = T_o + \delta T$ is usually written

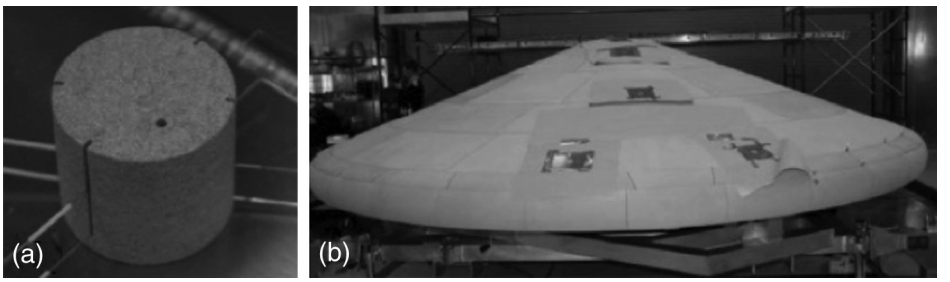

Fig. 1 (a) MEDLI instrumented sensor plug (MISP) with multiple wires. (b) MISPs installed in MSL flight heat-shield—source: Ref. 6.

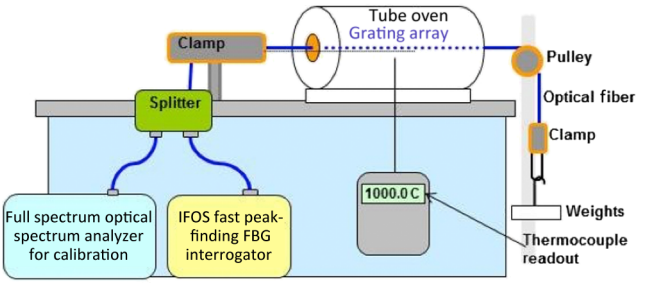

Fig. 2 Temperature characterization setup for assessing the temperature performance of gratings and conducting strain tests by providing tension on the fiber gratings with hanging weights.

$$\delta\lambda_B = \lambda_B(\xi + \alpha)\delta T, \tag{1}$$

where α is the thermal expansion coefficient, and ξ is the thermo-optic coefficient of the optical fiber. The coefficient of thermal expansion and thermo-optic coefficient of silica at room temperature are known to be $\alpha = 0.55 \times 10^{-6}/°C$ and $\xi = 8.6 \times 10^{-6}/°C$, respectively, which results in a theoretical temperature dependent wavelength shift of ~13.7 pm/°C near 1500 nm around room temperature for a typical FBG. However, in general, ξ is a function of temperature, and this must be taken into account over the extended temperature ranges encountered by TPS. The nonlinear dependence of λ_B on δT can be written in the form

$$\lambda_B = \lambda_{Bo} + a_1\delta T + a_2\delta T^2 + \ldots \tag{2}$$

Alternatively, if wavelength is measured, then temperature T can be determined using an expansion of the form

$$T = T_o + b_1\delta\lambda_B + b_2\delta\lambda_B^2 + \ldots \tag{3}$$

where b_n are experimentally determined calibration coefficients. Explicit second and third-order expansions for T are given for example fibers in Secs. 2.3 and 2.4.

2.2 *Test Setup for Fiber Bragg Grating Characterization*

Schematic of Fig. 2 and the photographs of Fig. 3 are the setup that was implemented to determine the basic temperature (and strain)-dependent properties of the FBGs, with a focus on determining fractional wavelength shift as a function of temperature.

2.3 *Calibration of High-Temperature Fiber Bragg Grating Array to 1000°C*

The objective was to demonstrate survivability of a grating array (fabricated for measuring differential temperatures) at elevated temperature. We also wanted to show survivability when subjected to tensile loading during and after high-temperature treatment as some tensile loading may occur during a heat-shield operation, and degradation of strength would not be desirable in such circumstances. The array consisted of two type II-IR gratings with room-temperature wavelengths of ~1529 and 1549 nm in "self-clad" fiber (with a large diameter silica cladding). This array was taken to nearly 1000°C over a period of 85 min, and subjected to ~6.8 ksi of tensile force (applied by hanging 0.6 kg to the end of the fiber) without breaking. Figure 4 shows the spectrum of the two-FBG array for several temperatures. We note a shift of ~13 nm as the temperature is increased from room temperature to close to 1000°C.

The thermocouple response and FBG wavelength shift as a function of time are plotted in Fig. 5. We observe a similar time response in both data sets, as expected.

The calibration obtained from this test is plotted in Fig. 6. A third-order polynomial given in Fig. 6 was used to fit the FBG temperature response data in the temperature range from 33 up to 1000°C. Rewriting in terms of a typical room temperature of 22.5°C gives for these type II-IR FBGs:

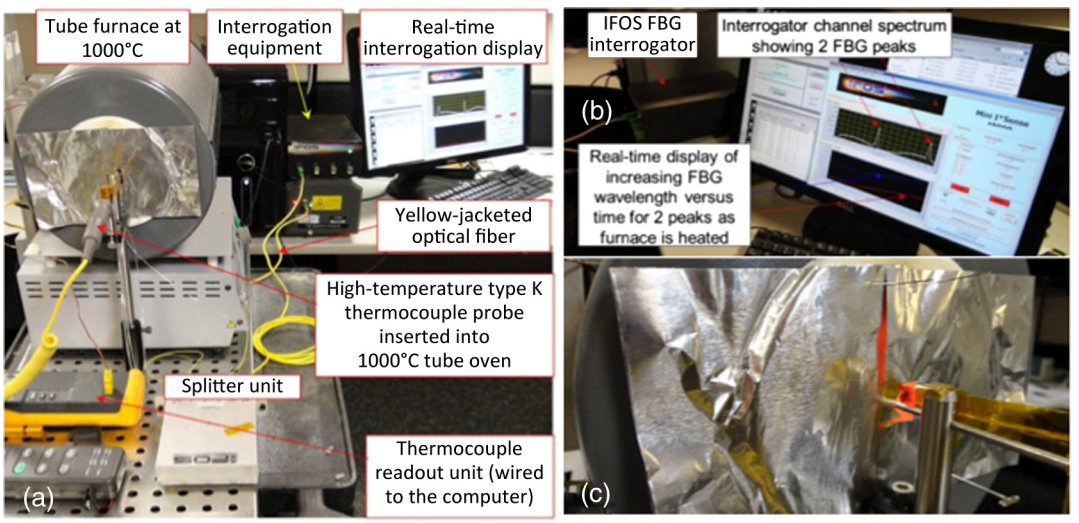

Fig. 3 (a) Setup for FBG characterization to 1000°C tests showing furnace, interrogation equipment, and display. (b) Zoom of FBG interrogation readout showing real-time tracking of FBG wavelengths. (c) One end of furnace at 1000°C with reference thermocouple probe and FBG sensor array inserted through the foil covering.

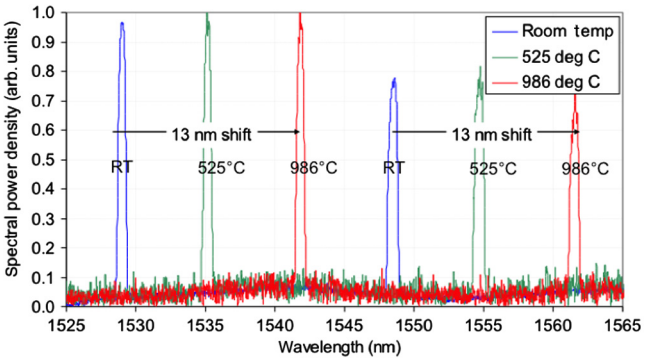

Fig. 4 FBG array spectrum for several temperatures.

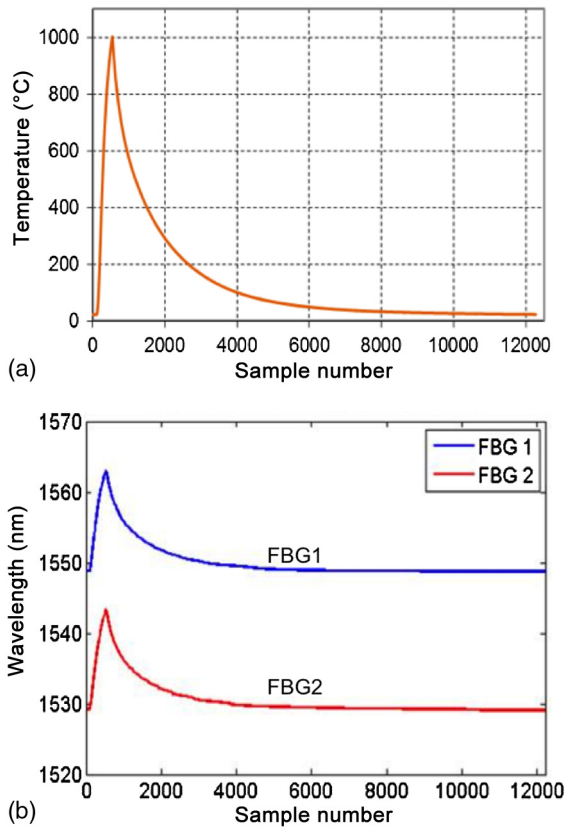

Fig. 5 (a) Thermocouple temperature versus time. (b) FBG wavelength vs time (2 s/sample).

$$T/^{\circ}\mathrm{C} = 22.5 + 1.5648 \times 10^{5}(\delta\lambda_B/\lambda_B) - 1.0926 \times 10^{7}(\delta\lambda_B/\lambda_B)^2 + 6.17 \times 10^{8}(\delta\lambda_B/\lambda_B)^3 \quad \text{to } 1000^{\circ}\mathrm{C} \tag{4}$$

While at 990°C, we subjected the FBG array to 6.78 ksi tensile stress (46.7 MPa) by hanging 600 g on the end of the fiber. Following cooling, we subjected the FBG array to 18.1 ksi tensile stress by suspending 1.6 kg on the end of the fiber without any signs of breakage.

2.4 *Calibration of Fiber Bragg Grating Arrays for SLA Experiments to 300°C*

Using the setup of Figs. 2 and 3, we also characterized the temperature dependence of two of the type I FBGs to be used for the SLA experiments described in Sec. 3. For this smaller temperature range, we found that the temperature dependence was well approximated by a second-order polynomial as shown in Fig. 7 for the two FBGs—the fractional wavelength dependence is almost identical for each of them. This result forms the basis of the wavelength-to-temperature conversion used to generate the temperature versus time plots at the end of Sec. 3. Rewriting in terms of a typical room temperature of 22.5°C gives for these type I FBGs

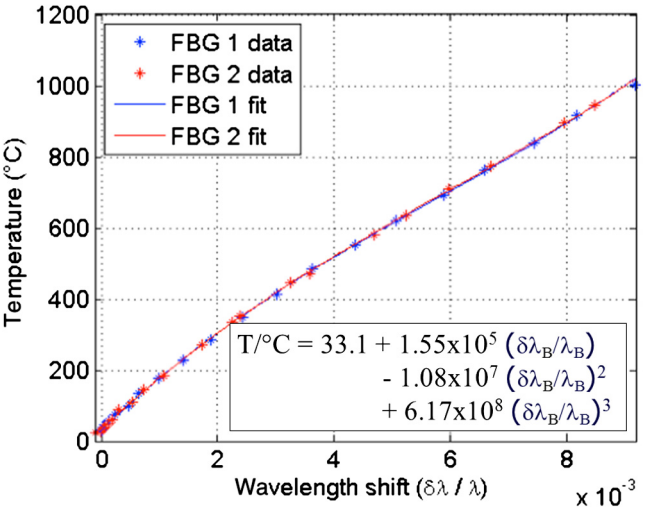

Fig. 6 Calibration curve for high-temperature FBGs deduced from the results in Fig. 5.

$$T/^{\circ}\mathrm{C} = 22.5 + 1.5887 \times 10^{5}(\delta\lambda_B/\lambda_B) - 1.56 \times 10^{7}(\delta\lambda_B/\lambda_B)^2 \quad \text{to } 300^{\circ}\mathrm{C}. \tag{5}$$

Comparison with of type-I results of Sec. 2.4 with type II-IR results of Sec. 2.3: For both types of FBGs, we find the empirical rule of thumb that to lowest order:

$$\delta T \sim 1.6^{\circ}\mathrm{C} \times 10^{5}\delta\lambda_B/\lambda_B, \tag{6}$$

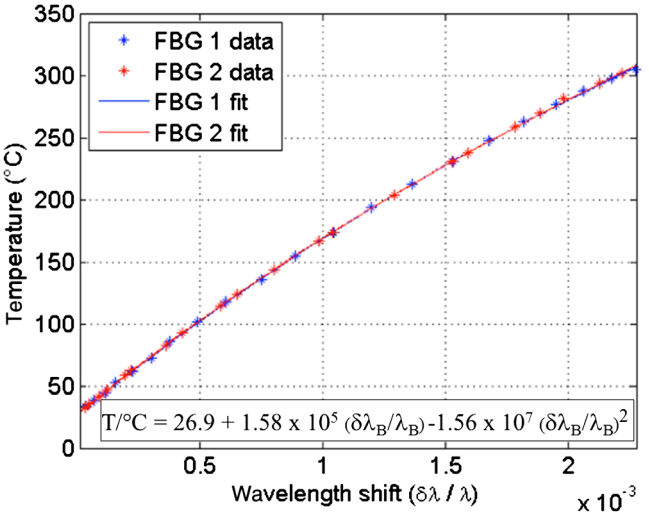

Fig. 7 Temperature versus fractional wavelength shift for two of the FBGs used for the SLA tests.

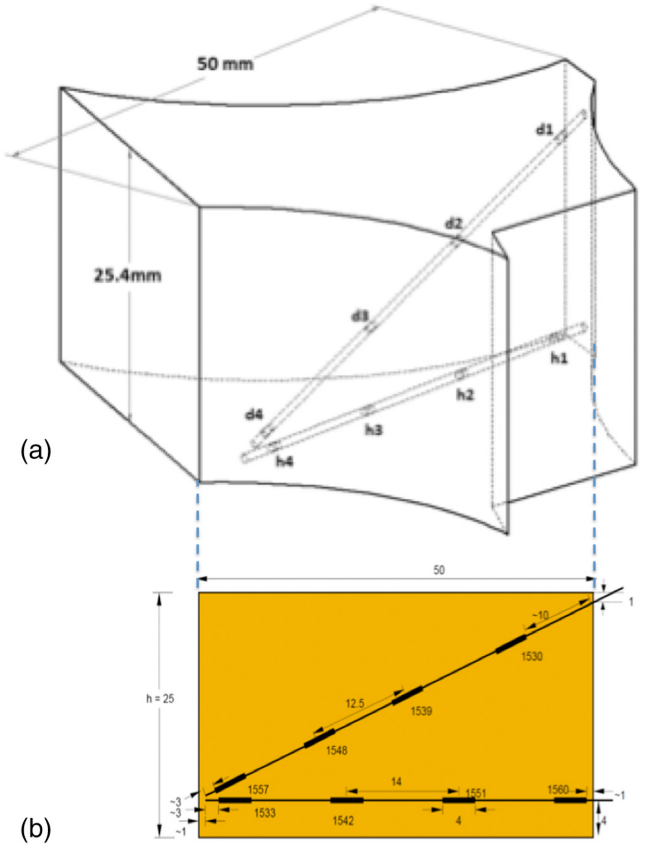

Fig. 8 (a) Sketch of SLA TPS sample with embedded optical fiber sensors. (b) Vertical cross-section showing placement of FBG sensors in TPS sample in the plane of the optical fibers as seen in Fig. 7(a). FBG wavelengths are indicated in nanometers and dimensions are in millimeters.

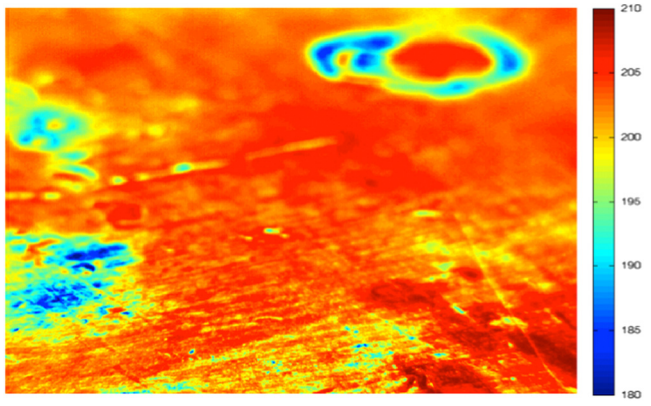

Fig. 9 IR thermal image of lower platen once heated (colors represent temperature in °C indicated on the right).

i.e., a fractional wavelength change of 10^{-5} implies ~1.6°C temperature change for strain-free FBGs, which at 1550 nm translates to the well-known order-of-magnitude result of ~0.1°C per picometer of wavelength change. This dependence, however, can depend significantly on temperature as discussed in the Appendix and seen in the example results of Fig. 17.

We also remark that over the range from room temperature to 300°C, as can be understood from the quadratic terms in Eqs. (4) and (5), a slightly larger nonlinear wavelength shift per °C of temperature change is seen for the type I FBG measurement results of Fig. 7 versus the type II-IR FBGs of in Fig. 6.

3 Sensorized Thermal Protection System Coupon

A single-SLA specimen was sensorized with two arrays of four annealed type-I FBG sensors. The SLA specimen, provided by NASA/ARC, had the dimensions shown in the CAD drawing of Fig. 8(a). In these experiments, the specimen was heated on the bottom surface, whereas the top surface was unheated to provide a thermal gradient through the TPS material.

Two arrays of FBG sensors were first embedded into the specimen. One array was parallel to the bottom surface at a depth of 4 mm and the other was angled as shown in Fig. 8(b). The FBG sensors in the horizontal sensor array were labeled h1 to h4. Similarly, the FBG sensors in the diagonal sensor array were labeled d1 to d4. Note that sensor h1 was extremely close to the edge of the specimen. It was, therefore, expected that the temperature measurements from this sensor would be noisy due to convection along the outer edge of the specimen. This expectation is supported by the experimental results presented in Sec 4.

4 Thermal Loading of Thermal Protection System Coupon

Two sets of temperature loading tests were performed on the SLA sample.

In the "first set of tests," the maximum applied temperature was limited to 250°C to prevent char of the material. In the 22 to 250°C temperature range, the temperature control of a hot-press (used for composite laminate manufacturing) was able to maintain the required temperatures. The specimen was place on the lower platen which was heated to 200°C. The upper platen was not heated and the two platens were separated the maximum distance so as to not affect the airflow around the specimen. Active cooling of the platens was not used. Therefore, the lower platen temperature was independently measured with a noncontact infrared thermometer before the specimen was placed on the platen. At

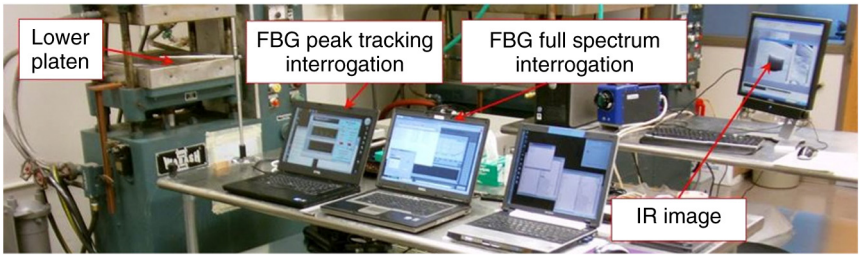

Fig. 10 Photograph of test specimen on hot platen. The optical fibers were supported by the stainless steel rod in the foreground to prevent them from touching the platen.

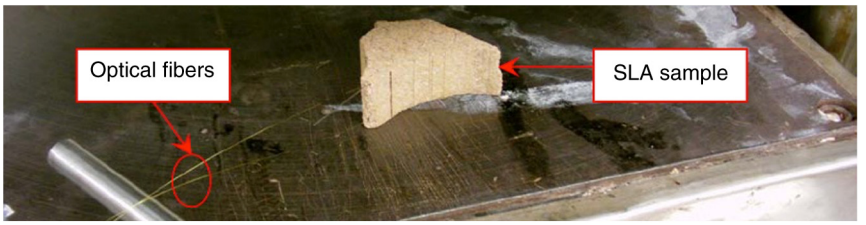

Fig. 11 Photograph of instrumentation during testing. The computer on the left was connected to the main IFOS interrogator used to track the grating wavelength peak. The center front computer was linked to a second IFOS interrogator which provided the full grating spectrum. The rear computer was attached to the IR camera.

the start of testing, the actual platen temperature at this point varied from 195 to 205°C between the individual tests.

For each test, the lower platen was heated until the temperature had stabilized. A location on the platen was marked such that the temperature was always measured at the same location, and the specimen was centered on this location. A thermal image of the lower platen was collected with an IR camera (Cedip Infrared Systems Titanium 560 M) to measure the temperature variations across the platen. Since the image was taken from the side of the hot-press, the image field of view that was in focus was limited. An example thermal image of the heated platen is shown in Fig. 9.

As instrumentation (Fig. 10), IFOS parallel processing peak tracking (I*Sense 48K) and full-spectrum (D*Sense) FBG interrogators were used. All FBG wavelengths were measured simultaneously with the I*Sense while the D*Sense, which provided backup and allowed verification of the FBG spectral forms. Since the temperature changes were expected to happen relatively slowly, sampling was at ~9 Hz. The I*Sense 48K system does, however, have the capability of sampling at up to 6 kHz.

For each test, the FBG instrumentation was activated, and then the TPS specimen was placed by hand onto the heated platen. The specimen was left on the platen for 5 min, then removed by hand and placed on a table. FBG sensor data were collected throughout the heating and cooling cycles. Figure 10 shows the specimen on the platen, and the instrumentation and the IR camera, whereas Fig. 11 shows the SLA specimen on the platen.

The thermal loading cycle was repeated twice (test 1-1, test 1-2) while allowing the specimen to completely cool between tests. Additionally, between the two tests, the instrumentation was disconnected from the specimen and shut down. Note that, as shown in Figs. 8 and 11, the two FBG sensor arrays only had two lead-in optical fibers for all eight sensors (compared to a much larger number for a similar thermocouple array). At one point during each test, once the specimen had reached steady-state thermal conditions, an infrared image of the specimen was taken with the IR camera.

Figure 13 shows the temperature versus time for each of the FBG sensors during test 1-1 and test 1-2. Each of the plots represents over 9000 data points. The temperatures reported in Fig. 13 assume the FBG fractional wavelength shift to temperature conversion of Fig. 7. Apart from the different timescales (a little over 15 min for test 1-1 and 21 min for test 1-2), the similarities are striking, lending confidence to the repeatability of the measurements. Other than for sensor h1, the response of each FBG was smooth and repeatable between the two tests. The large amount of noise in the response of FBG h1 was due to its location extremely close to the specimen edge, as described earlier.

The other three sensors in the horizontal array (h2, h3, h4) demonstrated a close response. Although each of these

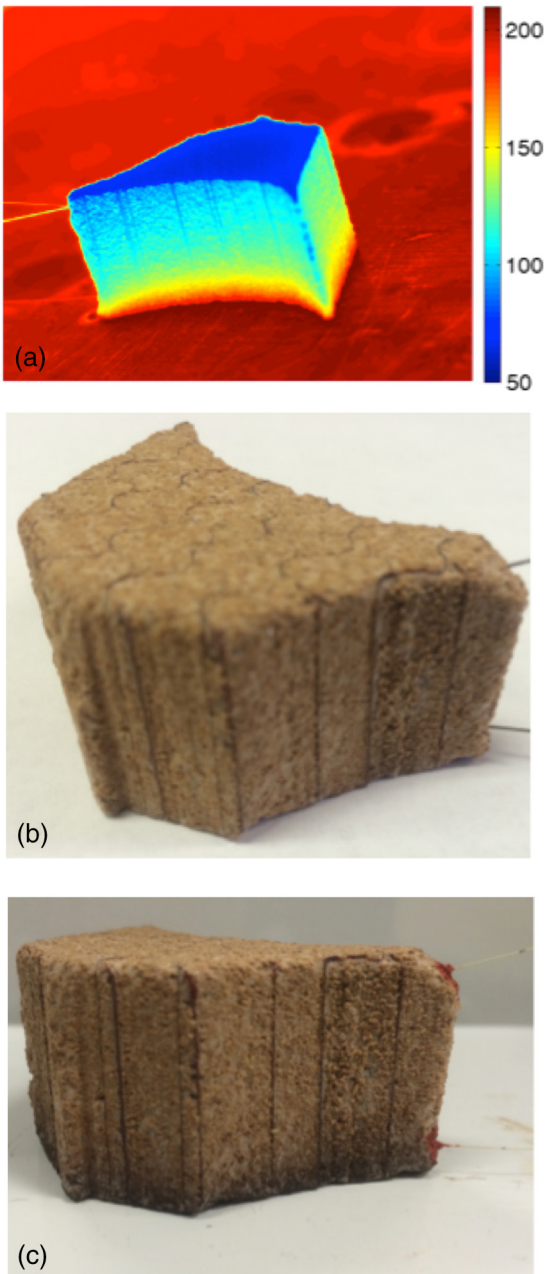

Fig. 12 SLA sample: (a) IR image at point of maximum temperature in test 1-2, (b) before and (c) after test 2-1 described below.

sensors is located at the same distance from the lower surface of the specimen, these results show that the temperature profile is not one-dimensional through the TPS specimen. Evidence of the effects of the specimen edges was also seen in infrared images of the SLA sample during testing, e.g., see Fig. 12(a).

After ~3.5 min, the temperature measurements of sensors d1, d2, d3, and d4 are in the expected order as a function of distance from the bottom surface of the specimen. In the initial heating phase, d1 measured a higher temperature than d2. This is probably due to the fact that although d1 is a further distance from the lower surface, it is also closer to the specimen vertical edge. In the cooling transient, we observe that d1 does cool at a slightly faster rate than d3 for the same reason. Of the sensors in the diagonal array, d2 and d3 are located the furthest from the vertical edges and are, therefore, the slowest to cool to room temperature.

The temperature measurement results of Figs. 13 to 15 demonstrate that the FBG sensor arrays can provide high spatial density temperature information as a function of time. In future work, we will compare these temperature measurements to those of thermocouple-instrumented plugs to better calibrate and quantify the accuracy of these spatially varying temperature measurements.

In the "second set of tests," a Thermolyne hotplate was used to heat the lower surface of the specimen. In the first two tests, the sample was placed on the hotplate for the entire duration of each test. In the first test (2-1) shown in Fig. 14(a), heating was maximized and the sample was allowed to reach above 250°C before the hotplate was turned off after ~8 min, resulting in light charring of the bottom of the sample. In the second test (2-2) shown in Fig. 14(b), the hotplate temperature dial was set to half maximum at $t = 1.4$ min and the temperature rise recorded until 3.4 min. These timescale zoom results further show the ability of the fiber-optic sensors to capture the temperature variation close to the SLA surface resulting from the temperature variation on the surface of hotplate, as well as variations in the bottom surface layer of the lightly charred SLA.

In tests 2-3 and 2-4, a procedure similar to that used with the hot press results of Fig. 13 was adopted with the sample being placed on and removed from the hotplate after preheating to slightly above 200°C. Results in Fig. 15 are similar to those in Fig. 13 except that the heating of the diagonal gratings with respect to the horizontal gratings is a little slower for the latter results, probably due to the lightly charred layer on the bottom of the sample [Fig. 12(c)] providing an increase in insulation with respect to the pristine sample [Fig. 12(b)] according to the process described in Sec. 1. Also note that in test 2-4, the sample was left on the hotplate long enough for all the horizontal array sensors to stabilize at constant temperatures.

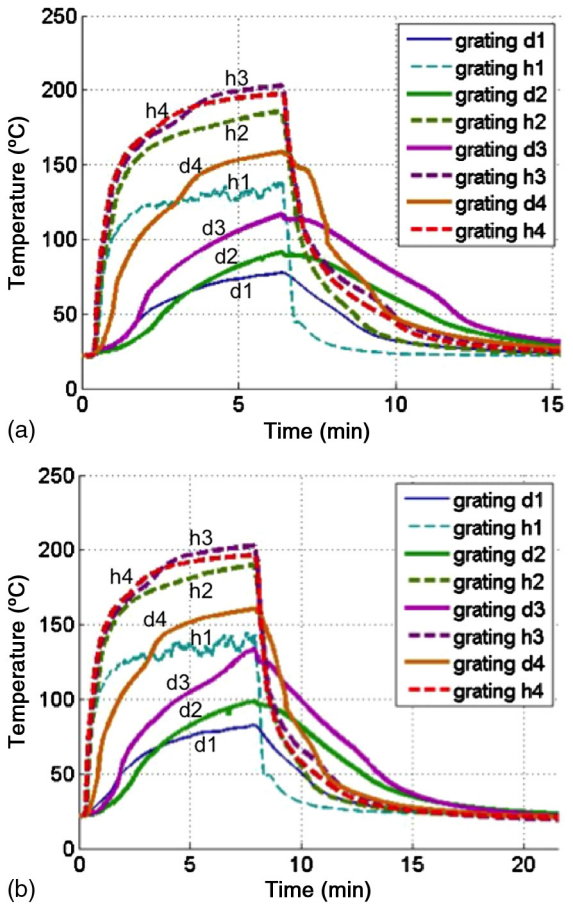

Fig. 13 Temperatures measured by FBG sensors for (a) test 1-1 and (b) test 1-2 with sample placed on hotpress for 6.7 and 8.3 min, respectively.

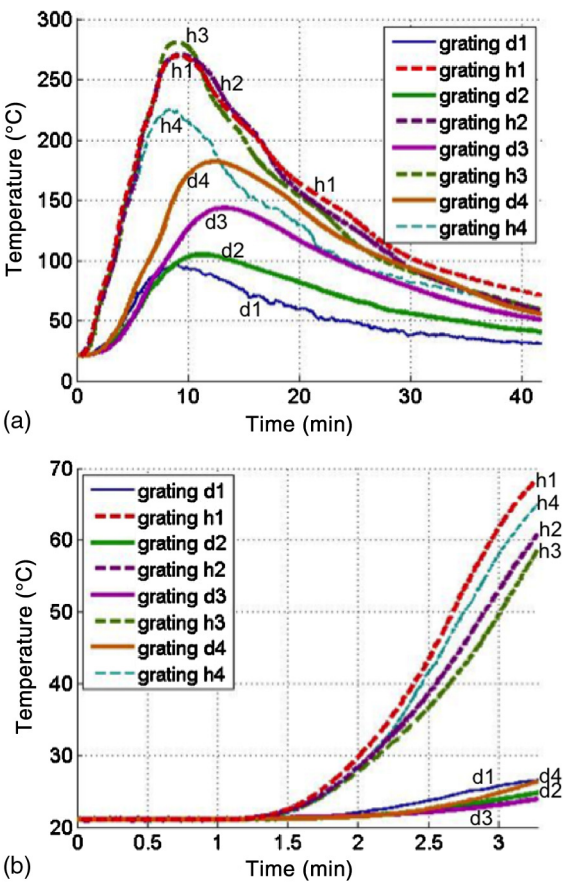

Fig. 14 Temperatures measured by FBG sensors for (a) test 2-1 and (b) test 2-2 with sample continuously on hotplate that was turned on near beginning of test.

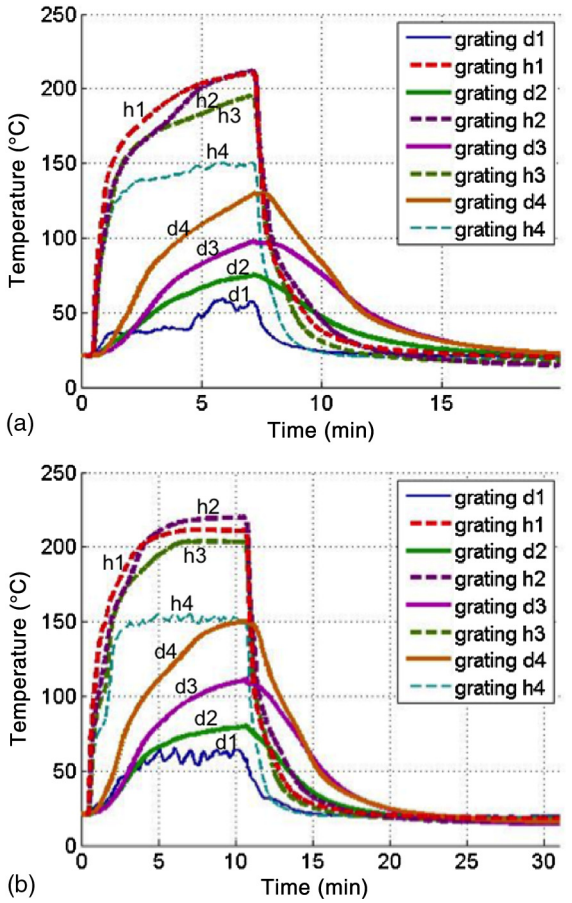

Fig. 15 Temperatures measured by FBG sensors for (a) test 2-3 and (b) test 2-4 with sample placed on hotplate for approximately 7 and 11 min, respectively.

5 Conclusions

The work reported in this paper was performed by IFOS and NCSU in the context of a NASA STTR project.[34] Highlights of the Phase 1 work included:

1. a demonstration of the survivability of FBG sensor arrays up to 1000°C;
2. a demonstration of the ability of the FBG sensor arrays to support some tensile loading while subjected to the same temperature range;
3. a calibration of the FBG response to pure thermal loading up to 1000°C;
4. the successful embedding of two FBG sensor arrays (a total of eight FBG sensors) in a small-size (maximum cross section 50 mm × 25 mm height) SLA TPS coupon with only two lead-in optical fibers;
5. the acquisition of temperature measurements from the two embedded FBG sensor arrays during thermal loading of the SLA TPS coupon. The temperature data were collected at both high spatial densities and high acquisition rates. While both the spatial density and data acquisition rate will be significantly increased in future experiments, these measurements clearly show the ability of FBG sensors, in connection with the IFOS interrogator, to capture thermal transients as they propagate through a TPS material; and
6. the use of multipoint FBG temperature measurements as a basis for heat flux measurement.[35]

The results demonstrate the potential of FBG sensor arrays and IFOS interrogator technology for embedded TPS instrumentation at high spatial and time resolutions. These measurements were obtained without the need for multiple lead wires, as would be typical for thermocouple sensor arrays. Finally, the thermal mass of silica is much closer to that of the TPS system than metallic sensors. This means that the perturbation of the heat flux measurement due to the thermal resistance difference between the sensor and TPS material is much lower, therefore, the measurements are more accurate. This closer matching of the thermal properties means that we will actually be able to measure spatial differences in the heat flux, since the local thermal resistance perturbation does not "smear" over these variations. Additionally, since the optical fiber does not have electrical current running through it, it does not locally heat up and perturb the local heat flux field that we are trying to measure.

While this paper focuses on temperature gradients determined by multiple FBGs with each FBG giving a single temperature (that may be considered as "averaged" over its length), a complementary paper in this volume[36] considers the determination of temperature gradient information over the length of a single FBG.

Appendix: Calibration over Extreme Temperature Range

For space applications, in addition to high temperatures experienced during atmospheric capture, very low temperatures may be experienced. We have compiled the following two composite graphs, Figs. 16 and 17, for unattached FBGs based on our measurements from Sec. 2.3 (25 to 1000°C for type II-IR FBGs) together with data given in Roth et al.[37] for cryogenic temperatures (down to close to absolute zero for a type I FBG) and Liao et al.[38] up to 1200 °C (for a type II-IR FBG). While these results can have some dependence on how the FBG was written, particularly for temperatures over 250°C (above which unannealed type I FBGs start to lose reflectivity), and especially over 700°C, Fig. 17 emphasizes the considerable temperature dependence of the term $\xi + \alpha$

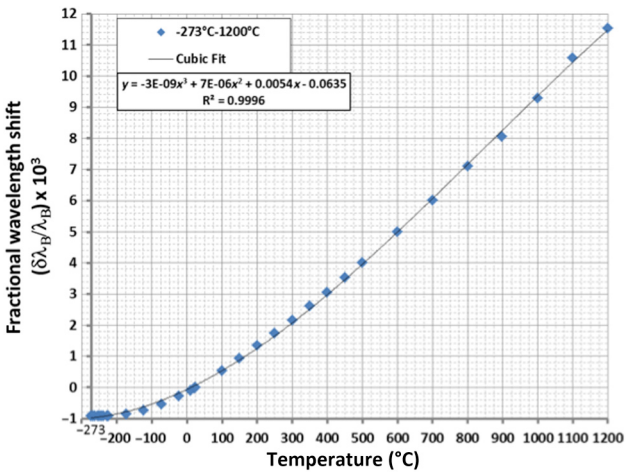

Fig. 16 Fractional wavelength shift (×10^3) over the range −273 to 1200°C with respect to 25°C.

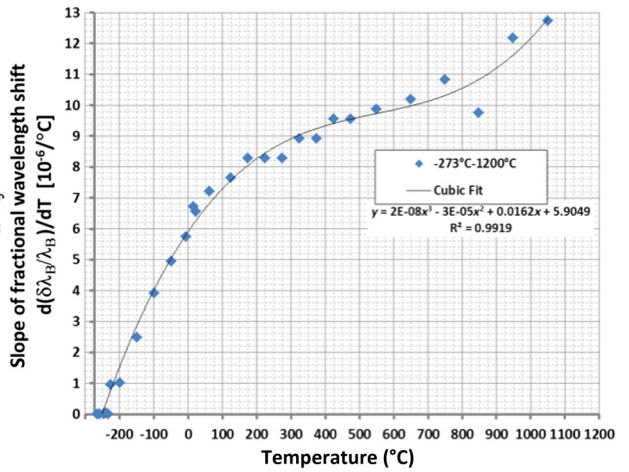

Fig. 17 Slope of fractional wavelength shift ($\times 10^6$) over the range −273 to 1050°C with respect to 25°C.

appearing in Eq. (1). While our focus has been on robust type II-IR FBGs,[21,39,40] annealed/regenerated FBGs[41–44] can also withstand high temperatures (9000 h at 890°C in Ref. 41) through to glass softening (1450 to 1500°C in Ref. 43). Their Bragg wavelengths also have a nonlinear temperature dependence.[44] Electric arc written long-period gratings (LPGs) have also been considered for high-temperature applications[24] and their wavelength transmission spectra exhibit significant temperature dependence with notch wavelengths that can decrease with temperature.[25] LPGs can also be laser written and in photonic crystal fibers have exhibited particularly interesting properties for sensing both temperature[26] and other parameters.[27] FBG approaches show advantages in multiplexing many sensors using only one end of the fiber, whereas LPGs require the source to be at the opposite end of the fiber to the detection while providing interesting possibilities for the discrimination of strain and temperature effects.

Acknowledgments

This research was funded by NASA through STTR contracts NNX11CI02P (Phase 1) and NNX12CB01C (Phase 2) to IFOS with NCSU as Research Institute subcontractor. We thank IFOS colleagues Ferey Faridian and Levy Oblea as well as Len LaCroix and NASA Ames Research Center personnel especially Donald T. Ellerby, Mary E. Livingston, Anuscheh Nawaz, and Joe G. Hartman for helpful feedback. This paper is an improved and expanded version of our previous SPIE conference proceedings paper.[45]

References

1. A. R. Howard, A. M. Cassell, and E. Venkatapathy, "Small probes as flight test beds for thermal protection materials," in *7th Int. Planetary Probe Workshop (IPPW-7)*, Barcelona, Spain (2010).
2. E. Venkatapathy et al., "Going beyond rigid aeroshells: enabling Venus in-situ science missions with deployables," in *8th Int. Planetary Probe Workshop (IPPW-8)*, p. 4, Portsmouth, Virginia (2011).
3. M. Stackpoole et al., "Post-flight evaluation of stardust sample return capsule forebody heatshield material," in *46th AIAA Aerospace Sciences Meeting and Exhibit*, AIAA, Reno, Nevada (2008).
4. P. Agrawal, J. F. Chavez-Garcia, and J. Pham, "Fracture in phenolic impregnated carbon ablator," *J. Spacecr. Rockets* **50**(4), 735–741 (2013).
5. A. Little et al., "The Mars Science Laboratory (MSL) Entry, Descent and Landing Instrumentation (MEDLI): hardware performance and data reconstruction," in *Atomic Absorption Spectroscopy*, pp. 13–078, NF1676L-15960 (2013).
6. A. Little et al., "The Mars Science Laboratory (MSL) Entry, Descent and Landing Instrumentation (MEDLI): hardware performance and data reconstruction," (2013).
7. E. Venkatapathy et al., "Selection and certification of TPS: constraints and considerations for Venus missions," in *6th Interplanetary Probe Workshop*, Atlanta, Georgia (2008).
8. E. L. Strauss, "Superlight ablative systems for Mars lander thermal protection," *J. Spacecr. Rockets* **4**(10), 1304–1309 (1967).
9. D. Driver et al., "Arc jet testing in a shear environment for Mars Science Laboratory thermal protection system," in *41st AIAA Thermophysics Conf.*, p. 4230, San Antonio, Texas (2009).
10. D. M. Driver et al., "Arcjet testing in shear environment for Mars Science Laboratory thermal protection system," *J. Spacecr. Rockets* **51**(4), 1151–1166 (2014).
11. D. A. Kontinos and M. J. Wright, "Introduction: atmospheric entry of the Stardust sample return capsule," *J. Spacecr. Rockets* **47**(5), 705–707 (2010).
12. C. Park, R. L. Jaffe, and H. Partridge, "Chemical-kinetic parameters of hyperbolic earth entry," *J. Thermophys. Heat Transfer* **15**(1), 76–90 (2001).
13. E. Venkatapathy et al., "Thermal protection system development, testing, and qualification for atmospheric probes and sample return missions: examples for Saturn, Titan and Stardust-type sample return," *Adv. Space Res.* **44**(1), 138–150 (2009).
14. E. Martinez and T. Oishi, "Current developments in sensors for thermal protection systems," in K. Fletcher, Ed., *5th European Workshop on Thermal Protection Systems and Hot Structures*, p. 28, ESA SP No. 631 (2006).
15. E. Martinez, E. Venkatapathy, and T. Oishi, "Current developments in future planetary probe sensors for TPS," A. Wilson, Ed., *Planetary Probe Atmospheric Entry and Descent Trajectory Analysis and Science*, pp. 249–252 (2003).
16. P. Wercinski et al., "Trajectory, aerothermal conditions, and thermal protection system mass for the MARS 2001 aerocapture mission," in *35th AIAA Aerospace Sciences Meeting & Exhibit*, p. 0472, Reno, Nevada (1997).
17. M. J. Gazarik et al., "Overview of the MEDLI Project," in *2008 IEEE Aerospace Conf.*, pp. 1–12 (2008).
18. D. Bose et al., "Mars 2020 entry, descent and landing instrumentation (MEDLI2)," (2016).
19. B. Moslehi et al., "Highly scalable operational sensor system for harsh environment applications," in *Proc. SAMPE*, Paper 57, pp. 2333–2314 (2012).
20. R. J. Black and B. Moslehi, "Advanced end-to-end fiber optic sensing systems for demanding environments (invited paper)," *Proc. SPIE* **7817**, 78170L (2010).
21. S. J. Mihailov, "Fiber Bragg grating sensors for harsh environments," *Sensors* **12**(2), 1898–1918 (2012).
22. M. N. Ott et al., "Applications of optical fiber assemblies in harsh environments: the journey past, present, and future," *Proc. SPIE* **7070**, 707009 (2008).
23. R. J. Black et al., "Fiber-optic sensing for thermal protection structures in vehicle health monitoring," in *Proc. Quantitative Non Destructive Evaluation (QNDE)* (2005).
24. R. J. Black et al., "High-temperature fiber optic sensors for integrated systems health management," in *Proc. 17th Aeromat Conf. and Exhibition* (2006), (invited paper).
25. R. J. Black et al., "Optical fiber gratings for structural health monitoring in high-temperature environments," *The 14th Int. Symp. on: Smart Structures and Materials and Nondestructive Evaluation and Health Monitoring*, Vol. **65308**, 65301P (2007).
26. A. Singh et al., "Temperature sensitivity of long period fiber grating in SMF-28 fiber," *Optik Int. J. Light Electron Opt.* **125**(1), 457–460 (2014).
27. S. Zheng, "Long-period fiber grating moisture sensor with nano-structured coatings for structural health monitoring," *Struct. Health Monit.* **14**(2), 148–157 (2014).
28. J. Wang et al., "Multiplexed high temperature sensing with sapphire fiber air gap-based extrinsic Fabry-Perot interferometers," *Opt. Lett.* **35**(5), 619–621 (2010).
29. R. J. Black et al., "Broadband fiber Bragg grating interrogation for structural health monitoring," in *SAMPE Baltimore 2015*, SAMPE, Baltimore (2015).
30. G. Hu, D. Chen, and X. Jiang, "Side-hole two-core microstructured optical fiber for hydrostatic pressure sensing," *Appl. Opt.* **51**(20), 4867–4872 (2012).
31. B. Moslehi and J. M. Costa, "Fiber optic pressure sensor based on differential signaling," U.S. Patent No. 8,402,834 (2013).
32. G. M. Flockhart et al., "Quadratic behavior of fiber Bragg grating temperature coefficients," *Appl. Opt.* **43**(13), 2744–2751 (2004).
33. G. Ghosh, "Sellmeier coefficients and dispersion of thermo-optic coefficients for some optical glasses," *Appl. Opt.* **36**(7), 1540–1546 (1997).
34. R. J. Black et al., "Fiber optic temperature sensors for thermal protection systems," in *Intelligent Fiber Optic Systems Corporation (IFOS)*, NASA, pp. 1–68 (2012).

35. D. A. Hackney et al., "Fiber bragg gratings for heat flux measurements in thermal protection systems under a steady conductive thermal load," in *ASME 2013 Conf. on Smart Materials, Adaptive Structures and Intelligent Systems*, pp. V002T05A009–V002T05A009 (2013).
36. D. A. Hackney et al., "Fiber Bragg gratings as transient thermal gradient sensors," *Opt. Eng.* **55**(11), 113102 (2016).
37. J. Roths et al., "Calibration of fiber Bragg cryogenic temperature sensors," in *Optical Fiber Sensors*, p. TuE81 (2006).
38. C. Liao et al., "Temporal thermal response of Type II-IR fiber Bragg gratings," *Appl. Opt.* **48**(16), 3001–3007 (2009).
39. S. J. Mihailov et al., "Bragg gratings written in all-SiO2 and Ge-doped core fibers with 800-nm femtosecond radiation and a phase mask," *J. Lightwave Technol.* **22**(1), 94–100 (2004).
40. R. B. Walker et al., "High temperature monitoring of an oxy-fuel fluidized bed combustor using femtosecond infrared laser written fiber Bragg gratings," *Proc. SPIE* **9754**, 975413 (2016).
41. G. Laffont, R. Cotillard, and P. Ferdinand, "9000 hours-long high temperature annealing of regenerated fiber Bragg gratings," *Proc. SPIE* **8794**, 87941X (2013).
42. G. Laffont, R. Cotillard, and P. Ferdinand, "Multiplexed regenerated fiber Bragg gratings for high-temperature measurement," *Meas. Sci. Technol.* **24**(9), 094010 (2013).
43. M. L. Åslund et al., "Rapid disappearance of regenerated fibre Bragg gratings at temperatures approaching 1500 C in boron-codoped germanosilicate optical fibre," in *(EWOFS'10) Fourth European Workshop on Optical Fibre Sensors*, Vol. **76534**, 76530Q (2010).
44. G. Adamovsky et al., "Peculiarities of thermo-optic coefficient under different temperature regimes in optical fibers containing fiber Bragg gratings," *Opt. Commun.* **285**(5), 766–773 (2012).
45. R. J. Black et al., "Fiber optic temperature profiling for thermal protection heat shields," *Proc. SPIE* **9062**, 906204 (2014).

Biographies for the authors are not available.